# Experimental and numerical study of the evolution of soot primary particles in a diffusion flame

Maria L. Botero[a], Nick Eaves[b], Jochen A.H. Dreyer[b], Yuan Sheng[c], Jethro Akroyd[b], Wenming Yang[a], Markus Kraft[c,*]

[a]*Department of Mechanical Engineering, National University of Singapore, 9 Engineering Drive 1, 117576, Singapore*
[b]*Department of Chemical Engineering and Biotechnology, University of Cambridge, Philippa Fawcett Drive, Cambridge, CB3 0AS, UK*
[c]*School of Chemical and Biomedical Engineering, Nanyang Technological University, 62 Nanyang Drive, 637459, Singapore*

**Abstract**

The evolution of primary soot particles is studied experimentally and numerically along the centreline of a co-flow laminar diffusion flame. Soot samples from a flame fueled with $C_2H_4$ are taken thermophoretically at different heights above the burner (HAB), their size and nano-structure are analysed through TEM. The experimental results suggest that after inception, the nascent soot particles coagulate and coalesce to form larger primary particles (∼5 to 15 nm). As these primary particles travel along the centreline, they grow mainly due coagulation and condensation and a layer of amorphous hydrocarbons (revealed by HRTEM) forms on their surface. This amorphous layer appears to promote the aggregation of primary particles to form fractal structures. Fast carbonisation of the amorphous layer leads to a graphitic-like shell around the particles. Further graphitisation

*Corresponding author:
*Email address:* mk306@cam.ac.uk (Markus Kraft)

compacts the primary particles, resulting in a decrease of their size. Towards the flame tip the primary particles decrease in size due to rapid oxidation. A detailed population balance model is used to investigate the mechanisms that are important for prediction of primary particle size distributions. Suggestions are made regarding future model development efforts. Simulation results indicate that the primary particle size distributions are very sensitive to the parameterisation of the coalescence and particle rounding processes. In contrast, the average primary particle size is less sensitive to these parameters. This demonstrates that achieving good predictions for the average primary particle size does not necessarily mean that the distribution has been accurately predicted.
*Keywords:*
Diffusion flame, soot, particle size distribution, population balance model

---

## 1. Introduction

Air pollution from carbon nanoparticles leads to respiratory disease and contributes to climate change. The smallest particles (below 100 nm) play a particularly important role in health since they penetrate the respiratory system deeper than larger particles [1] and dominate size distributions in terms of number concentration. In order to accurately predict the size distributions of soot particles it is necessary to understand the different processes involved in primary particle formation and growth. Numerical models must be able to accurately describe each of these steps to eventually mitigate soot emission.

The inception process, which is the transition from the gas to the first

nuclei, is still not completely understood. The smallest particles detected in flames are about 1–3 nm in diameter [2–4] and are thought to consists of PAH clusters [5] with 10–15 aromatic rings [6–9]. It is unclear whether these particles are nascent soot particles [3, 10] or soot precursor particles [11, 12]. These last ones have been found transparent to visible light [11] and sometimes they are described as "liquid-like" when observed under transmission electron microscopy (TEM), due to their low contrast [13–15], undefined boundaries and their deformation during thermophoretic sampling [2, 16, 17]. Recently, some researchers have been able to detect and measure these nascent soot particles using advanced techniques [3, 4, 10].

Laminar co-flow diffusion flames have been used extensively to study soot formation because they represent a simple analogue of more complex practical combustion systems. In these flames, the transition from precursor particles into solid nuclei is also debated. Some researchers have reported that the polydisperse precursor particles coagulate fast to form larger primary particles [11] and then carbonise [18] into solid monodisperse spherical particles via a mechanism that includes surface growth. The solid particles then aggregate to form larger fractal structures. Others reported the partial aggregation of the precursor particles before their complete solidification [14, 19]. Small solid nuclei form within large PAH-containing liquid-like particles [14, 17, 20], through carbonisation these liquid-like particles rapidly convert into small aggregates composed of mature primary particles [17] and further agglomerate to form larger fractal structures. Due to the complexity of the multiple processes that are taking place simultaneously in the flame, it is not yet possible to reconcile fully the influence of each process with

experimental observations of the growth of primary particles.

Several modeling studies in co-flow diffusion flames have been reported in the past 20 years. The majority of these investigations used population balance models (PBMs) that describe particles by one or two parameters (mass and number of primary particles or surface and volume) that are solved via sectional or moment methods. Two parameter models allow for a description of the fractal nature of soot aggregates; however, information regarding the primary particle size distribution (PPSD) within aggregates cannot be obtained. Previous numerical studies have focused on prediction of average primary particle size, partially due to the lack of experimental data on their number and size distributions, but also due to the limitations of the soot models implemented [21].

Herein, experimental and detailed modeling of the evolution of the primary particles of soot in a laminar diffusion flame of ethylene, is presented. The flame corresponds to one of the target flames defined at the International Sooting Flame (ISF) workshop for soot studies [22]. To the author's knowledge, this is the first time that experimental and simulated PPSD in a co-flow diffusion flame are reported. The presented methodology can be extended to other reactive flows. The growth of primary particles from single nascent precursor to mature particles in large aggregates is observed using TEM and simulated using a population balance model with a detailed description of the molecular and morphological structure of each particle (DPBM) [23, 24] and capable of resolving primary particle distributions within soot aggregates. Through the unique features of the soot model, a parametric sensitivity analysis is performed to challenge the understanding of the role of

various particle processes in the evolution of the soot primary particle size in the flame. Raw experimental data is provided in the supplementary material data to ease future modeling efforts by the community.

## 2. Experimental methods

The Yale burner [25] was used to generate a co-flow diffusion flame of ethylene diluted by nitrogen (60% vol $C_2H_4$ - 40% vol $N_2$), which corresponds to the ISF-3 Co-flow 3c [22]. Soot was sampled at different height above the burner (HAB) in the centreline using a fast-insertion thermophoretic sampling system [6]. For all the sampling positions, the exposure of the TEM grids was between 30-46 ms. Carbon-supported copper grids with a diameter of 3.05 mm were used to collect the soot samples. The samples were examined on a 200 kV JEOL 2100F TEM using a ZrO/W Schottky field emission gun. TEM images were taken with a magnification of 30,000x and 500,000x. The primary particle size was measured by fitting circles around the particles on each TEM image using a MATLAB code. More than 1000 primary particles were analysed at each sampling position. Contamination of the sample from large wing aggregates was estimated to be $\pm$15%. The flame temperature was measured with an uncoated R-type thermocouple with a wire diameter of 75 $\mu$m and corrected for radiation losses as detailed in [26]. Full details of the burner and sampling conditions can be found in the supplementary material.

## 3. Numerical Methods

The computational method consists of two parts as in previous studies. In the first part, velocity, and species profiles are computed using the CoFlame code, which includes a sectional description of the soot particle distribution and considers particle mass and number of primaries. The chemical mechanism in [27] is utilized along with PAH inception and condensation via benzo-a-pyrene (A5) [28], which is the largest PAH considered in the mechanism. The details of the CoFlame code can be found in [29] and previous works [30–33].

In the second part, a streamline corresponding to the centreline of the diffusion flame is generated from the CoFlame results and a detailed PBM is applied as a post-processing step. The post-processing methodology is well established and has been applied in a number of previous studies [34–36], although it should be noted that it cannot account for the effect of thermophoresis or diffusion of the particles. The experimental temperature profile is supplied as input along with shifting the profiles from the CoFlame code by 5 mm to match the experimental flame height. A brief description of the most important aspects of the detailed PBM is given below. Full details may be found elsewhere [24, 34, 35, 37]. The growth of PAH species within the model is described by a kinetic Monte-Carlo-aromatic-site (KMC-ARS) model [37], starting from benzo-a-pyrene. The dynamics of the soot particle population is described by the Smoluchowski equation with additional terms for particle inception, surface growth, oxidation, condensation, particle rounding, and sintering. In the model, soot particles are represented as aggregates composed of primary particles, where each primary particle is

composed of a number of PAHs [24]. A PAH is represented by the number of carbon and hydrogen atoms it contains, and the number and types of elementary sites on its edge [37]. Each aggregate stores a list of neighbouring primary particles and resolves the common surface area between each pair of neighbours, where each pair of neighbours can be in point contact, can be fully coalesced or can be anywhere in between [24]. The extent of contact between neighboring particles is described by a sintering level [38]. A sintering level of 0 corresponds to point contact. A sintering level of 1 corresponds to complete coalescence. The sintering level is increased via sintering and particle rounding processes. Sintering is modeled via the viscous flow model and is parametrised based on a pre-exponential factor $A_{\mathrm{s}}$, activation energy $E_{\mathrm{a}}$, and the critical diameter below which primaries are assumed to have nanostructural mobility ("liquid-like") and sinter instantaneously (coalescence), $d_{\mathrm{p,crit}}$. Particle rounding is the increase of sintering level due to condensation and surface growth reactions and is parameterised by the smoothing factor, $\sigma$. A value of 0 implies no rounding, while a value of 2 implies maximum rounding. A list of all the parameters utilized with the model can be found in the supplementary material.

## 4. Results and Discussion

### *4.1. Flame temperature*

Experimental and simulated temperature profiles at the centreline are presented in **Fig. 1**. The experimental temperature profile and maximum temperature measured in this study are consistent with the data reported by Smooke et al. [39]. However, our experimental results are slightly shifted

towards higher HAB, possibly due to the definition of the zero HAB and the difficulties to insert the thermocouple very close to the burner rim. At low HAB, the predicted temperature is significantly lower than the measurements, which was also reported for previous modeling efforts of this flame [40]. The simulated peak temperature is 100 K larger and is also shifted to larger HAB. The simulated temperature profile was then shifted by -5 mm in order to match the HAB at which the maximum temperature is obtained, resulting in a better agreement between the computations and experiments.

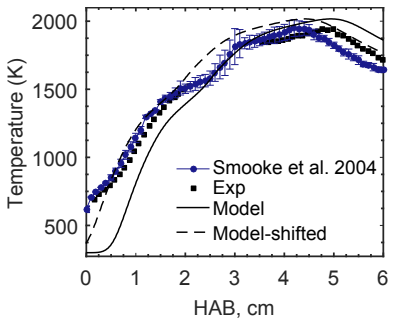


Figure 1: Temperature profile at the centreline of the flame. Experimental and numerical results.

### *4.2. Soot morphology*

The evolution of soot morphology along the flame centreline is presented in **Figure 2** including the mean primary particle diameter $\langle d_{PP} \rangle$ and estimated standard error. Soot is first detected at 10 mm HAB and consists of small single particles with an average size of 11 nm. The smallest particles that could be detected were between 4-5 nm. A small degree of aggregation is observed with almost complete coalescence, indicating that these particles may be formed from the coalescence of smaller particles [41, 42]. Some of

these nascent particles have low contrast and blurred boundaries whereas others present high-contrast and well-defined boundaries. HRTEM images reveal that they exhibit a short-range degree of nano-structural order and also a slight spreading on the substrate film (**Figure 3**).

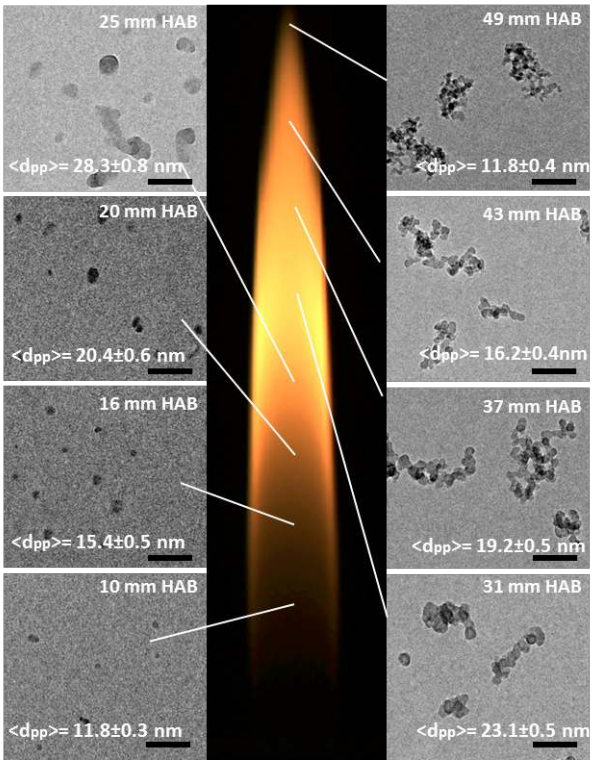


Figure 2: Representative TEM images showing the evolution of soot morphology in the flame. Left: soot images at low-medium HAB, Right: soot images at medium-large HAB. Each image contains the mean primary particle diameter at the corresponding HAB. Scale bar of 100 nm.

Downstream (16 to 20 mm HAB), the primary particles grow to sizes between 13 nm and 25 nm and consist mostly of single particles with some initial signs of aggregation. Different degrees of contrast are also observed, some of

them present the low-contrast reported by other researchers as "transparent-like", and some present a high contrast associated with solid particles. High resolution images of these particles show that they possess a higher degree of nano-structural order (**Figure 3**). We do not assume these particles to be true liquids, but only that they possess some nano-structural mobility under flame conditions [43].

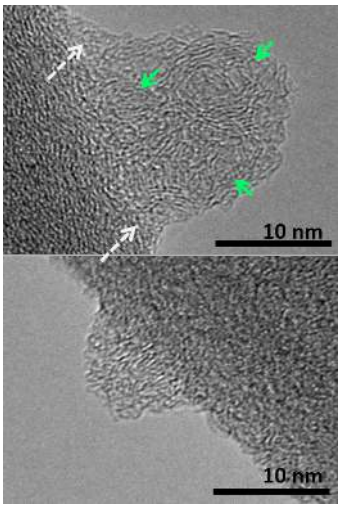


Figure 3: Representative HRTEM images of smallest soot particles sampled at 10 mm HAB, showing a short-range nano-structural order and internal nano-structures of smaller nascent particles (green arrows). Slight spreading can be observed in the edges of particle-grid contact (white-dashed arrows).

At 25 mm HAB (and to a lesser extent at 20 mm HAB) the aggregates have irregular shapes with a combination of well-defined spherical-like primaries and irregular structures. HRTEM images of these particles show that they consist of soot particles with some graphitic order surrounded by a layer of an amorphous carbon material. This explains the lower contrast of the particles on the edges and joints [44] (**Figure 4**). Chemical speciation of in-

cipient soot particles with similar morphology was performed by Blevins et al. [44], Öktem et al. [45], using laser desorption and solvent extraction followed by mass spectrometry. Their results show that the species desorbed from the particles are mainly composed of small PAHs (3-5 rings) and aliphatic molecules. The HRTEM images reveal that the small nascent primary particles at low HAB do not have the same nanostructure as the amorphous ("liquid-like") carbon condensed around the larger primaries at intermediate HAB.

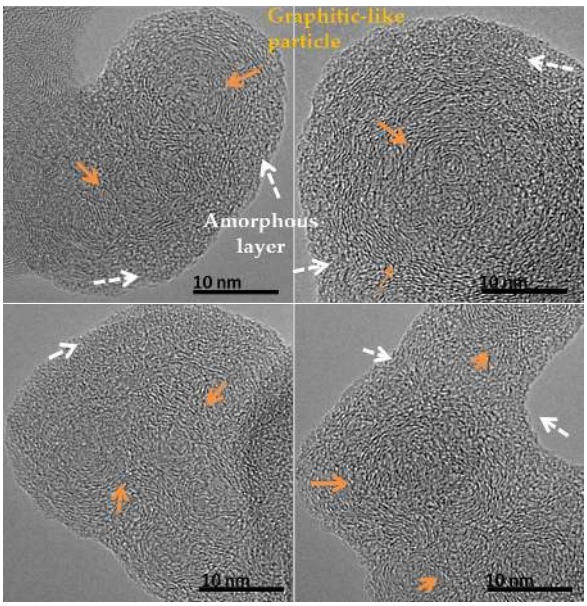


Figure 4: HRTEM images of soot sampled at 25 mm HAB showing existence of an amorphous carbon layer (white dashed arrow) surrounding the semi-graphitic solid particles (orange arrows).

Liquid-like patches surrounding the particles were observed at intermediate HAB (25 mm) and were found to be dependent on the sampling time (images can be found in the supplementary material), as reported by Khol-

ghy et al. [17]. As the exposure time of the TEM grid to the flame decreases, these liquid-like blobs become smaller until they disappear, suggesting less condensation of hydrocarbons with high boiling points on the sampling grid [44]. In our measurements, it was possible to avoid this condensible material with sufficiently short exposure times.

Further downstream, at 31 mm HAB larger aggregates with high-contrast and well-defined spherical shape are found. HRTEM images at this HAB (**Figure 5**) evidence the fast graphitisation of the previously condensed amorphous layer, forming a graphitic-like layer around the particles, probably due to the higher flame temperatures [17]. A slight decrease in the primary particle size is encountered suggesting a decrease in surface growth and compaction of the primary particles triggered by the increase in graphitisation [17, 19, 46]. Towards the top of the flame, the aggregate size remains fairly constant whilst the primary particle size consistently decreases. At the tip of the flame, both aggregate and primary particle size decrease substantially, due to soot oxidation [47–50].

### *4.3. Primary particle size distribution*

Experimental and simulated PPSDs at different HAB are presented in **Figure 6**. A kernel density estimation was used to generate the probability distribution function using a bandwidth of 2 nm. The detection limit in the experimental data is approximately 4 nm for single primaries (due to the poor contrast). Experimental results show that the PPSD shifts progressively to larger sizes and becomes wider from 10 to 25 mm HAB due to a combination of growth processes, then it shifts back to smaller sizes and narrows from 31 to 49 mm HAB due to combined graphitisation and oxidation. At all

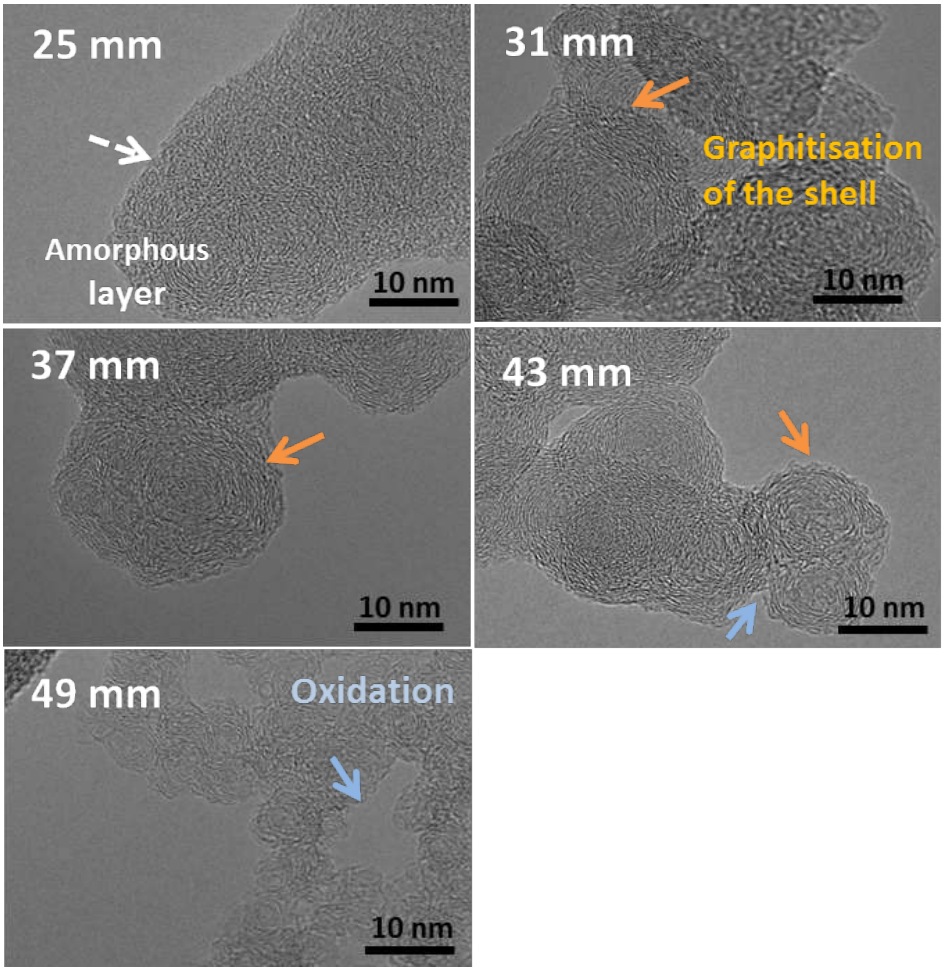


Figure 5: Representative HRTEM images of soot sampled at the flame centreline showing the evolution of the nano-structure of soot primary particle during growth and oxidation.

HAB, the PPSD is unimodal with a narrow width. At 25 mm HAB were a second mode of large particles slightly emerges; however, at this HAB the spherical primary particle size measured cannot fully represent the complex morphology of the aggregates described in the previous section.

There are many hypothesised mechanisms that contribute to the growth

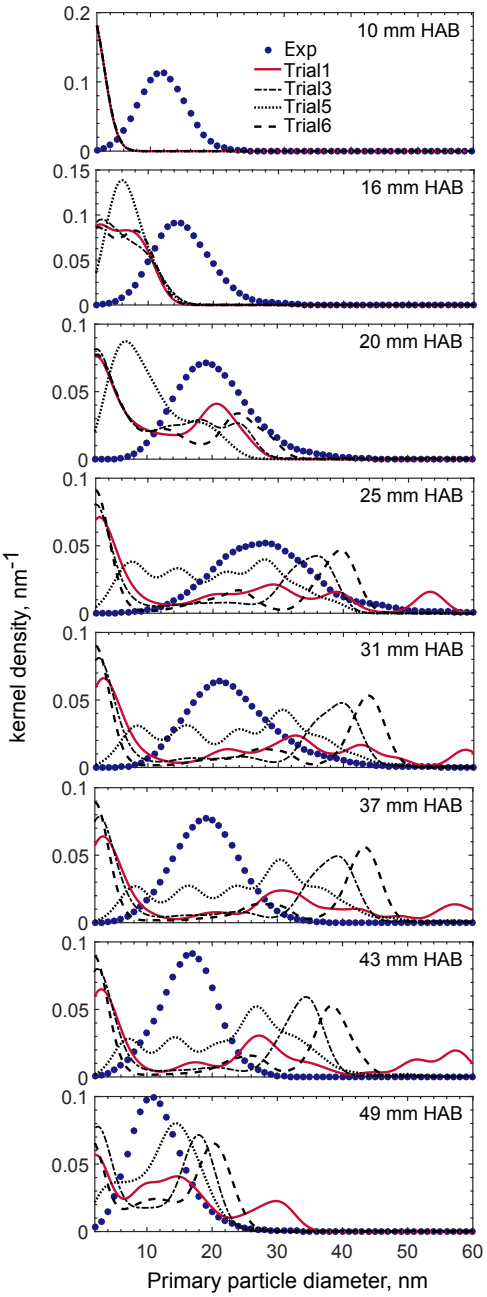


Figure 6: Experimental and simulated primary particle size distribution at different HAB. Trial 1: base case, Trial 3: reduce sintering pre-factor, Trial 5: increase coalescence critical diameter, Trial 6: reduce smoothing factor

of primary particles, such as sintering, particle rounding, and coalescence of liquid particles, all of which are described in the detailed PBM. This is the first time experimental data for the full PPSD is available, which allows the use of the PBM to challenge the accepted hypotheses. A sensitivity analysis is performed in order to understand the mechanisms that are important to the prediction of primary particle sizes and their contributions. The parameters that are investigated are 1) the sintering pre-factor ($A_s$), 2) critical diameter for instantaneous coalescence $d_{pri,crit}$, and 3) the smoothing factor ($\sigma$). Table 1 lists the parameters for each trial.

Table 1: Parameters for each trial run for the detailed population balance model (DPBM).

| **Trial** | $A_{\mathbf{s}}$ (s m$^{-1}$) | $d_{\mathbf{p,crit}}$ (nm) | $\sigma$ |
|---|---|---|---|
| 1 | 1.1 $\times 10^{-14}$ | 1.58 | 1.69 |
| 2 | 1.1 $\times 10^{-13}$ | 1.58 | 1.69 |
| 3 | 1.1 $\times 10^{-12}$ | 1.58 | 1.69 |
| 4 | 1.1 $\times 10^{-14}$ | 3 | 1.69 |
| 5 | 1.1 $\times 10^{-14}$ | 5 | 1.69 |
| 6 | 1.1 $\times 10^{-14}$ | 1.58 | 1.0 |
| 7 | 1.1 $\times 10^{-14}$ | 1.58 | 0.5 |

Before moving to the PPSDs, the commonly investigated average primary particle size and standard deviation are briefly discussed. **Figure 7** displays the experimental and numerical results for average primary particle size and standard deviation versus HAB (to be consistent with experimental limitations, only simulated particles larger than 4 nm were included). The numerical results show modest sensitivity to the investigated parame-

ters when considering the average size, whereas the standard deviation is more sensitive.

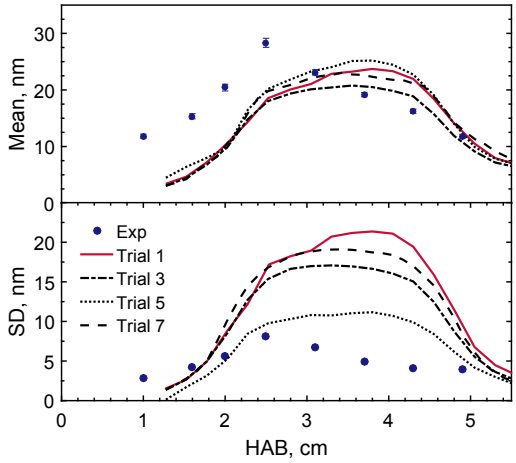


Figure 7: (a) Mean and (b) standard deviation of primary particle size at different HAB. Comparison of experimental and simulation results.

Although the model is capable of reasonably reproducing the trends in average size, it does not capture the experimental PPSD. In **Figure 6**, simulated PPSD results of selected trials are compared with experimental results. Results of all the trials can be found in the supplementary material. At all HABs, the numerical results exhibit a large mode of sub 2 nm primary particles. Additionally, results are shifted towards larger sizes and display a multi-modal character at higher HAB. The PPSDs show marked, and differing, sensitivity to all investigated parameters:

- Reducing the sintering pre-factor (Trials 2 and 3, see Fig. S3) reduces the multimodality at large HAB and causes the predicted PPSDs to become uni-modal. A very large sintering pre-factor results in the complete coalescence of sticking primary particles, resulting in the rapid

transition of aggregates back to spherical particles of equivalent mass, which increases the multimodality of the PPSD. A low sintering prefactor would prevent particles from merging, such that they persist as aggregates. The experimental evidence suggests that sintering should be strong in the inception region and decrease as the particles travel through the flame.

- Increasing the critical diameter for coalescence, $d_{\mathrm{p,crit}}$ (Trials 4 and 5, see Fig. S4a), eliminates the larger mode of sub 2 nm primaries and the modes at larger primary particle sizes at high HAB. This parameter represents the nano-structural mobility exhibited by nascent soot particles (so called "liquid-like" behavior in the literature), which facilitates their coalescence with larger particles.
- Reductions in the smoothing factor (Trials 6 and 7, see Fig. S4b) causes the predicted PPSDs to become bi- rather than multi-modal. The smoothing factor controls the rate of rounding due to molecules sticking to the particle surface. Thus, if it is too high, every surface growth reaction or condensation event would result in the complete rounding of neighbour particles into an spherical primary particle, resulting in a multi-modal PPSD. If the smoothing factor is too low, condensation and surface reactions would lead only to surface growth of the primary particle where the event takes place. This reduces the multimodality and allows the particles to remain as aggregates; however, it promotes the preferential surface growth of some particles, leading to a bi-modal distribution with a very pronounced mode of large primary particles.

Overall, these results display that while multiple hypotheses of the contri-

butions of various mechanisms can provide reasonable, and similar, results for average size, the same is not true regarding the PPSD. A summary of the influence of the model parameters on the predicted PPSDs is show in **Figure 8**. It is important to highlight that this is the first attempt to use a detailed model that resolves the connections between individual primary particles to test hypotheses about the processes involved in the formation and aggregation of primary particles. The experimental observations presented in this paper enables such models to be challenged and define specific aspects for future development.

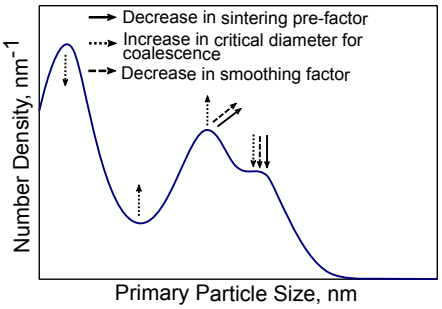


Figure 8: Summary of effects of key model parameters on predicted primary particle size distributions (PPSDs).

## 5. Conclusions

The evolution of the primary particle size distribution (PPSD) of soot in a co-flow diffusion flame was investigated experimentally and numerically, for the first time. Experimental results show that the smallest soot particles detected (4-5 nm) are formed by the coalescence of smaller nascent soot particles. These primary particles grow in size through coagulation and surface

growth (including condensation of small hydrocarbon species). The amorphous hydrocarbons condensed on the particle surface hereby seem to aid the aggregation process. We do not assume these particles to be true liquids, but rather that their surface possesses some nano-structural mobility under flame conditions. The amorphous layer graphitise due to the higher flame temperatures and starts forming a graphitic-like layer around the particles as evidenced by HRTEM images. Towards the flame tip the particles are oxidised. The experimental PPSD is mono-modal at all HAB with a narrow width. During the growth of particles the PPSD shifts to larger sizes and widens. During the shrinkage of particles, the PPSD shifts to smaller sizes and narrows. The predicted PPSDs by the detailed PBM are sensitive to the sintering pre-factor, critical diameter for "liquid-like" behavior, and smoothing factor, while average sizes are not sensitive. This demonstrates that reasonable prediction of average sizes does not ensure reasonable prediction of the distribution.

## Acknowledgments

This project is funded by the National Research Foundation (NRF), Prime Minister's Office, Singapore under its Campus for Research Excellence and Technological Enterprise (CREATE) programme.

## References

[1] K. BéruBé, D. Balharry, K. Sexton, L. Koshy, T. Jones, Clinical and Experimental Pharmacology and Physiology 34 (2007) 1044–1050.

[2] A. Abid, N. Heinz, E. Tolmachoff, D. Phares, C. Campbell, H. Wang, Combustion and Flame 154 (2008) 775–788.

[3] M. Schenk, S. Lieb, H. Vieker, A. Beyer, A. Gölzhäuser, H. Wang, K. Kohse-Höinghaus, ChemPhysChem 14 (2013) 3248–3254.

[4] T. Mouton, X. Mercier, M. Wartel, N. Lamoureux, P. Desgroux, Applied Physics B 112 (2013) 369–379.

[5] P. Elvati, A. Violi, Proceedings of the Combustion Institute 34 (2013) 1837 – 1843.

[6] M. L. Botero, D. Chen, S. González-Calera, D. Jefferson, M. Kraft, Carbon 96 (2016) 459–473.

[7] E. M. Adkins, J. H. Miller, Physical Chemistry Chemical Physics 17 (2015) 2686–2695.

[8] M. L. Botero, E. M. Adkins, S. González-Calera, H. Miller, M. Kraft, Combustion and Flame 164 (2016) 250–258.

[9] J. Lighty, V. Romano, A. Sarofim, H. Bockhorn, A. D'Anna, A. Sarofim, H. Wang, Combustion Generated Fine Carbonaceous Particles, KIT Scientific Publishing (2009) 487–500.

[10] C. Betrancourt, F. Liu, P. Desgroux, X. Mercier, A. Faccinetto, M. Salamanca, L. Ruwe, K. Kohse-Höinghaus, D. Emmrich, A. Beyer, A. Gölzhäuser, T. Tritscher, Aerosol Science and Technology 51 (2017) 916–935.

[11] A. D'Anna, A. Rolando, C. Allouis, P. Minutolo, A. D'Alessio, Proceedings of the Combustion Institute 30 (2005) 1449 – 1456.

[12] S. Di Stasio, J. B. a. Mitchell, J. L. Legarrec, L. Biennier, M. Wulff, Carbon 44 (2006) 1267–1279.

[13] A. D'Anna, A. Ciajolo, M. Alfè, B. Apicella, A. Tregrossi, Proceedings of the Combustion Institute 32 (2009) 803 – 810.

[14] U. O. Koylu, C. S. McEnally, D. E. Rosner, L. D. Pfefferle, Combustion and Flame 110 (1997) 494–507.

[15] R. Dobbins, R. Fletcher, H.-C. Chang, Combustion and Flame 115 (1998) 285–298.

[16] A. C. Barone, A. D. Alessio, A. D'Anna, Combustion and Flame 132 (2003) 181–187.

[17] M. Kholghy, M. Saffaripour, C. Yip, M. J. Thomson, Combustion and Flame 160 (2013) 2119–2130.

[18] J. Lahaye, G. Prado, J. B. Donnet, I. M. Kennedy, Carbon 12 (1974) 27–35.

[19] R. L. V. Wal, Combustion Science and Technology 118 (1996) 343–360.

[20] P. T. A. Reilly, R. A. Gieray, W. B. Whitten, J. M. Ramsey, Combustion and Flame 122 (2000) 90–104.

[21] W. J. Menz, M. Kraft, Aerosol Science and Technology 47 (2013) 734–745.

[22] I. S. F. Workshop, Laminar flames - co-flow laminar diffusion flame, https://www.adelaide.edu.au/cet/isfworkshop/data-sets/laminar/, 2017.

[23] E. K. Y. Yapp, M. Kraft, Modelling Soot Formation: Model of Particle Formation, Springer London, London, pp. 389–407.

[24] M. Sander, R. I. Patterson, A. Braumann, A. Raj, M. Kraft, Proceedings of the Combustion Institute 33 (2011) 675 – 683.

[25] J. Gau, D. Das, C. McEnally, D. Giassi, N. Kempema, M. Long, Yale coflow diffusion flames steady flame burner, http://guilford.eng.yale.edu/yalecoflowflames/steady_burner.html, ????

[26] M. L. Botero, S. Mosbach, J. Akroyd, M. Kraft, Fuel 153 (2015) 31 – 39.

[27] S. B. Dworkin, Q. Zhang, M. J. Thomson, N. A. Slavinskaya, U. Riedel, Combustion and Flame 158 (2011) 1682–1695.

[28] N. A. Eaves, S. B. Dworkin, M. J. Thomson, Proceedings of the Combustion Institute 35 (2015) 1787–1794.

[29] N. A. Eaves, Q. Zhang, F. Liu, H. Guo, S. B. Dworkin, M. J. Thomson, Computer Physics Communications 207 (2016) 464–477.

[30] N. A. Eaves, A. Veshkini, C. Riese, Q. Zhang, S. B. Dworkin, M. J. Thomson, Combustion and Flame 159 (2012) 3179–3190.

[31] N. A. Eaves, M. J. Thomson, S. B. Dworkin, Combustion Theory and Modelling 185 (2013) 1799–1819.

[32] N. A. Eaves, S. B. Dworkin, M. J. Thomson, Proceedings of the Combustion Institute 36 (2017) 935–945.

[33] A. Khosousi, F. Liu, S. B. Dworkin, N. A. Eaves, M. J. Thomson, X. He, Y. Dai, Y. Gao, F. Liu, S. Shuai, J. Wang, Combustion and Flame 162 (2015) 3925–3933.

[34] E. K. Y. Yapp, R. I. A. Patterson, J. Akroyd, S. Mosbach, E. M. Adkins, J. Houston Miller, M. Kraft, Combustion and Flame 167 (2016) 320–334.

[35] D. Chen, Z. Zainuddin, E. Yapp, J. Akroyd, S. Mosbach, M. Kraft, Proceedings of the Combustion Institute 34 (2013) 1827 – 1835.

[36] E. K. Y. Yapp, D. Chen, J. Akroyd, S. Mosbach, M. Kraft, J. Camacho, H. Wang, Combustion and Flame 162 (2015) 2569–2581.

[37] A. Raj, M. Celnik, R. Shirley, M. Sander, R. Patterson, R. West, M. Kraft, Combustion and Flame 156 (2009) 896 – 913.

[38] M. Sander, R. H. West, M. S. Celnik, M. Kraft, Aerosol Science and Technology 43 (2009) 978–989.

[39] M. D. Smooke, R. J. Hall, M. B. Colket, J. Fielding, M. B. Long, C. S. McEnally, L. D. Pfefferle, Combustion Theory and Modelling 8 (2004) 593–606.

[40] M. D. Smooke, M. B. Long, B. C. Connelly, M. B. Colket, R. J. Hall, Combustion and Flame 143 (2005) 613–628.

[41] P. A. Mitchell, M. Frenklach Ph.D. (2001) 317 p.

[42] N. Morgan, M. Kraft, M. Balthasar, D. Wong, M. Frenklach, P. Mitchell, Proceedings of the Combustion Institute 31 (2007) 693 – 700.

[43] R. H. Hurt, G. P. Crawford, H.-S. Shim 28 (2000) 2539–2546.

[44] L. G. Blevins, R. a. Fletcher, B. a. Benner, E. B. Steel, G. W. Mulholland, Proceedings of the Combustion Institute 29 (2002) 2325–2333.

[45] B. Öktem, M. P. Tolocka, B. Zhao, H. Wang, M. V. Johnston, Combustion and Flame 142 (2005) 364 – 373.

[46] R. Dobbins, Aerosol Science and Technology 41 (2007) 485–496.

[47] I. M. Kennedy, Progress in Energy and Combustion Science 23 (1997) 95–132.

[48] Z. Li, L. Qiu, X. Cheng, Y. Li, H. Wu, Fuel 211 (2018) 517 – 528.

[49] M. L. Botero, S. Mosbach, M. Kraft, Fuel 126 (2014) 8 – 15.

[50] M. L. Botero, S. Mosbach, M. Kraft, Fuel 169 (2016) 111 – 119.

**Supplemental Material**

**Click here to download Supplemental Material: supplementary.pdf**

**Supplemental Material**

**Click here to download Supplemental Material: SupplMat-PrimaryParticleSize.csv**

**Supplemental Material**

**Click here to download Supplemental Material: SupplMat-Temperature.csv**